A Study of RF Dosimetry from Exposure to an AMI Smart Meter

Lanchuan Zhou and John B. Schneider

School of Electrical Engineering and Computer Science
Washington State University
Pullman, WA 99164-2752
E-mail: lzhou@eecs.wsu.edu; schneidj@eecs.wsu.edu

Abstract

As part of the development of the advanced metering infrastructure (AMI), i.e., the "smart grid," power utilities are increasingly deploying residential meters that wirelessly communicate (either with devices in the home, with other meters, or with the utility). These meters may employ multiple antennas and radiate at different frequencies, ranging from 850 MHz to 2.4 GHz. Unlike radio-frequency (RF) exposure caused by cell phones, where the position of the phone relative to the body is somewhat fixed, the position of a power meter relative to the body is rather unconstrained. In this work, we used the Finite-Difference Time-Domain (FDTD) Method to study the Specific Absorption Rate (SAR) produced in full anatomical models of humans when they were exposed to the RF fields produced by a wireless AMI meter, commonly referred to as a smart meter. Various scenarios were considered, most of which could be described as "beyond worst case." Despite this fact, only when an individual was extremely close to one particular radiating element *and* when one ignored the actual duty cycle of these meters did the SAR values exceed the published safety limits. When one accounts for the meter's true duty cycle *or* there was a realistic separation between the meter and an individual, all SAR values fell within safety limits.

Keywords: Dosimetry; specific absorption rate; finite difference methods; electromagnetic radiation effects

1. Introduction

The smart grid – or, more formally, the advanced metering infrastructure (AMI) – has as one of its key components meters that can wirelessly communicate. These meters are commonly referred to as smart meters. These meters can communicate with devices within the home, with other AMI meters, or with the electric power utility. The deployment of these meters has not been without concern on the part of some citizens, e.g., [1-3]. These concerns center on the possible health effects that may be caused by exposure to the non-ionizing radio-frequency (RF) fields produced by these meters.

An extensive study of the fields associated with an Itron smart meter has recently been reported [4]. This study analyzed the fields produced by these meters using measured data. The meter was studied in a host of settings, including a residential home, an apartment building (where a bank of meters was installed), the laboratory, and an outdoor test facility (where approximately 7000 meters were present). This measured data showed that in realistic scenarios, the exposure a human would receive was well below the maximum permissible exposure limits.

In this work, we used the Finite-Difference Time-Domain (FDTD) method [5, 6] to study RF dosimetry in humans exposed to one particular smart meter. This dosimetry was quantified by obtaining the specific absorption rate (SAR) induced in full anatomical models of various humans. The 1 g, 10 g, and whole-body averaged SAR values were obtained and compared to basic restrictions of relevant safety standards. In many ways, the results presented here represented "beyond worst case" scenarios, in that the simulations involved distances between the human and the meter that were not likely to occur in practice; the simulations assumed the maximum transmitted power from a *cell-relay* meter; and the simulations did not account for the small duty cycle associated with typical data transmissions. In practice, wireless smart meters transmit for short durations. Benefiting from CDMA EVDO high-data-rate technology, the average duty cycle for the cellular transceiver in a cell relay is approximately 0.088% [4]. Note that a *cell-relay* meter communicates data obtained from the mesh-network of meters back to the electric utility via a wireless wide-area network (WWAN) using cellular-telephone technology. Typically, one cell-relay meter services between 500 and 750 "end-point" meters in a given network. End-point meters lack the dual-band antenna (considered below) that is found in cell-relay meters, and hence end-point meters radiate less total power than cell-relay meters.

The FDTD method is a full-wave, time-domain solver for Maxwell's equations. It is robust, accurate, and well suited to studying problems involving highly inhomogeneous media, such as the human body. The FDTD method has been used numerous times to study human exposure to various radiating devices, e.g., cell phones [7-13], mobile-phone base-station antennas [14], Wi-Fi [15] and Bluetooth devices [16], and "electronic article surveillance" devices [17]. The FDTD method has also been extensively used to study exposure to plane waves, e.g., [18-20].

In this work, we characterized the exposure via the specific absorption (SAR) rate, for which there are published standards [21, 22]. No further attempt was made to characterize the health effects of the electromagnetic fields. For a discussion of health issues that goes beyond the SAR value, the interested reader is referred to [23, 24]. The SAR uncertainties from effects of age-dependent tissue variations [11], posture, and anatomical variations [18, 25] have been studied previously, and are beyond the scope of the current analysis. However, we do wish to point out that [11] showed that age-dependent tissue variation had little effect on the peak spatially average SAR value.

In the remainder of this work, we start by describing the model of the smart meter that was incorporated into the FDTD simulation. We then provide an overview of the FDTD implementation that was used. This is followed by the results obtained from a number of numerical experiments. We then provide conclusions.

2. Implementation

2.1 Meter Model

An AMI smart meter is shown in Figure 1. This particular meter might be described as atypical, in that it is designed to collect information from other meters and relay this information back to the utility. Such a meter might thus represent perhaps one out of every 500 to 750 meters that are deployed in a geographic region. We selected this meter to study since it radiates more power than end-point meters (i.e., meters attached to residences that do not contain cell-relay functionality). The meter box (or "socket") has the dimensions of the box shown in the figure. The wireless communication with the utility is via the dual-band antenna that is mounted on the inside of the transparent meter cover. This antenna is visible in Figure 1 as a black patch on the left side of the cover. When active, the dual-

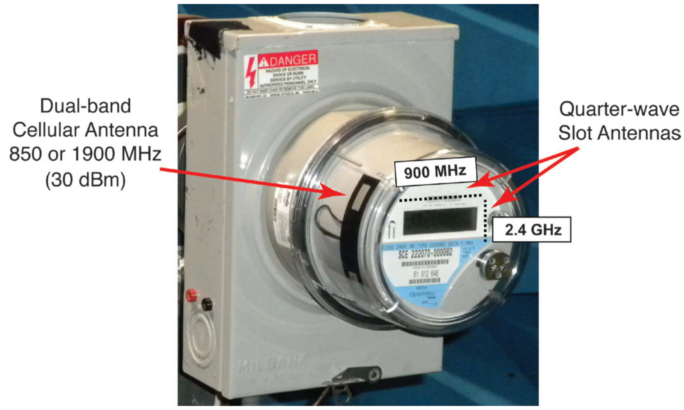

Figure 1. A picture of the AMI meter that served as the basis for the simulations done in this work. The black patch shown on the left side of the meter cover is the dual-band antenna studied in this work (photo courtesy of Richard Tell).

band antenna was assumed to radiate 30 dBm (one watt) at either 850 MHz or 1900 MHz. There are two additional antennas present in this particular meter. They are both quarter-wave slot-line antennas that are incorporated into the circuit boards behind the meter's front face. The horizontal slot-line antenna radiates approximately 24 dBm at 900 MHz (75% less than the dual-band antenna). The vertical slot-line antenna radiates approximately 20 dBm at 2.4 GHz (90% less than the dual-band antenna). Owing to the fact that the dual-band antenna radiates the most power, it was the antenna considered in this work. In practice, the duty cycle for this antenna is small ($\approx$ 0.088% [4]). Nevertheless, all the calculations presented here assumed steady-steady radiation (i.e., the antenna was always radiating full power).

Figure 2 shows a detailed view of the dual-band antenna used in the FDTD simulations. Some approximations of the actual antenna were made. First, the actual antenna is slightly curved as it follows the contour of the meter cover. In the simulations to follow the antenna was assumed to exist in a plane. The spatial step size used in the FDTD simulations was 1.5 mm. For some of the metal traces of the antenna, this required a slight modification of the dimensions in order to conform to the underlying FDTD grid, but never by more than half a millimeter. (For example, the long, thin "wings" of the antenna were 1.5 mm wide in the FDTD simulations, instead of their actual width of 1.0 mm. The more important dimensions in the model were those of the 15 mm and 47 mm segments of these wings. The length of the 15 mm segment was exactly modeled, whereas the 47 mm segment was modeled as 46.5 mm.) In the FDTD simulation, the antenna was driven with an additive current source between the two black circular dots that appear toward the center of Figure 2. (The cable that attaches to these points on the actual antenna is partially visible on the side of the meter in Figure 1.)

In the FDTD simulations, the antenna was placed in front of a meter box at a distance corresponding to the distance found

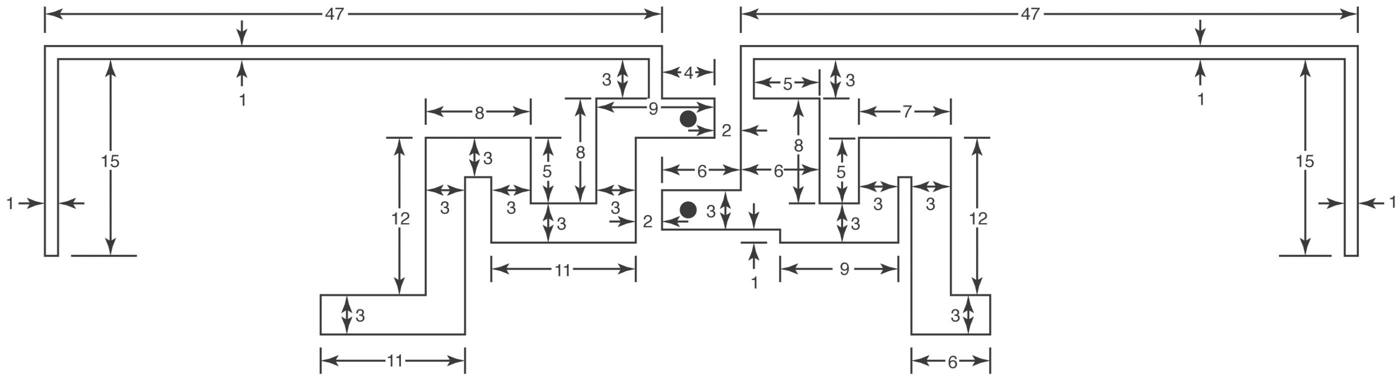

Figure 2. The layout of the dual-band antenna. All dimensions are in millimeters. The black outline shows the area that was treated as metal within the FDTD simulations. The antenna was assumed to be planar, and hence was realized by setting to zero the electric-field nodes that fell within the black outline.

in the actual meter. Additionally, the offset of the antenna from the center of the meter was taken into account. The meter box was treated as a perfect electric conductor (PEC). The dimensions used for the box were those of a Milbank U7487-RL socket: 3.625 in × 8 in × 11.5 in (corresponding to the depth, width, and height, respectively). The circular hole in the front face was incorporated into the model, but the hole that appears at the top of the meter box in Figure 1 was not. The electronics in the actual meter were not modeled. The meter model thus consisted of the radiating antenna positioned in front of the meter box. The radiation pattern of the meter shown in Figure 1 was measured and also calculated via the FDTD method. The measured and calculated patterns were roughly equivalent, sharing similar features, with neither pattern exhibiting strong directionality.

2.2 FDTD Implementation

The underlying FDTD "computational engine" used in this work employed the standard second-order Yee algorithm [5, 6]. The FDTD code was written in-house. The FDTD grid was terminated with an eight-cell convolutional perfectly matched layer (CPML) [26, 27]. A convolutional perfectly matched layer of six cells has previously been shown to be effective in a wide variety of SAR calculations [28]. The eight-cell convolutional perfectly matched layer used in this work thus should have been more than adequate for the scenarios considered. In order to facilitate the investigation of large problems, the code used the *Message Passing Interface* (*MPI*) in order to distribute the computation over a cluster of computers [29].

The problem was discretized using a uniform spatial step size of 1.5 mm. This ensured at least 10 points per wavelength within the material with the highest relative permittivity. Simulations were run at the three-dimensional Courant limit of $1/\sqrt{3}$, i.e., $S_c = c\Delta t/\Delta\delta = 1/\sqrt{3}$ where S_c is the Courant number, c is the speed of light, Δt is the temporal step size, and $\Delta\delta$ is the spatial step size in the x, y, and z directions.

As previously mentioned, the antenna was excited by placing an additive current source across the two black circular dots shown in Figure 2. Once the simulation began, the source function was harmonic at the frequency of interest. Actually, it was quasi-harmonic since – to help minimize the spectral content at frequencies that were not of interest – the amplitude was ramped up gradually, using an exponential envelope where the amplitude reached 99% of its asymptotic limit after 10 cycles. Specifically, the amplitude was given by $1-\exp\left(-S_c n/2N_\lambda\right)$, where n is the integer time step, and N_λ is the (free-space) number of points per wavelength, which was 105 for 1900 MHz and 235 for 850 MHz.

Simulations were typically run for 10,000 time steps, which was sufficient to ensure that steady-state had been achieved. Most of the body tissues had relative permittivities around 55 at 850 MHz and 1900 MHz. For this permittivity, over the duration of the simulation, a field can propagate 1.17 m (equivalent to traversing the body more than twice, if the body was less than 50 cm in depth). Even with the highest relative permittivity – 70 for gallbladder at 850 MHz – the field could propagate more than 1 m over the duration of the simulation. Given the loss in the tissue, these lengths/durations were sufficient to obtain steady-state. Moreover, the existence of steady-state was also verified by checking the magnitude and phase of the field at various points throughout the computational domain. After 10,000 time steps, the variations in the magnitude and phase from one cycle to the next were found to be less than two percent.

The simulations were constructed so that the dual-band antenna radiated a total of one watt. This was achieved by first doing a simulation involving just the antenna. A current source of known amplitude was applied to the antenna, and then the total radiated power was calculated [30]. Given this relationship between current and radiated power, the amplitude of the current was then scaled to obtain one watt of radiated paper.

The humans in the simulation were members of the Virtual Family [31]. This “family” consists of a 34-year-old male (Duke), a 26-year-old female (Ella), an 11-year-old female (Billie), and a 6-year-old male (Thelonious). Instead of using the names of the jazz greats as given in [31], in the spirit of a family we will refer to these four as Dad, Mom, Daughter, and Son, respectively. The composition of the members of the Virtual Family was defined via continuous boundaries between different materials (by “materials,” we mean those present in a human, e.g., grey matter, muscle, bone, and internal air). In this way, the FDTD modeler can specify any spatial sample size, and the Virtual-Family software will report the type of material that exists at each sample point. From a Web site maintained by the Italian National Research Council [32], after merely specifying the frequency of interest, one can obtain the relative permittivity and conductivity that pertain to each material (and hence, to each sample point).

As mentioned above, in the simulations done here, the spatial step size was 1.5 mm. However, the Virtual-Family software was used to obtain voxel models sampled at 0.75 mm. In accordance with the approach described in [33, 34], the data from this “sub-sampled” person were then used to determine the coefficients that appeared in the FDTD update equations using a spatial step size of 1.5 mm.

In various instances, such as when the meter was directly in front of the nose, we performed two simulations: one with the entire body, and one with just the upper torso. We found that the peak SAR values were identical for the two different simulations. We thus concluded portions of the body that were “far” from the location of the peak SAR had little to no effect on the SAR. Consequently, we did not study the effect of a ground plane, since the geometric spreading of the field from the finite source was likely to ensure that any fields reflected from a ground plane would be small compared to the direct field.

The specific absorption rate (SAR) requires the calculation of the square magnitude of the electric field, i.e.,

$$\mathrm{SAR} = \sigma \frac{|\mathbf{E}|^2}{2\rho}, \tag{1}$$

where σ is the conductivity, ρ is the density, and the vector electric field, $\mathbf{E}$, has components $E_x \hat{\mathbf{a}}_x + E_y \hat{\mathbf{a}}_y + E_z \hat{\mathbf{a}}_z$. In the FDTD method, the field components are offset in space so that none of the electric-field components are spatially collocated. Different algorithms have been proposed to handle this spatial offset [19, 35-37]. In this work, the SAR was calculated at the corner of a voxel. Assuming the voxel had indices (i, j, k) and the x, y, and z components of the electric field were each offset a half spatial step in the direction in which they pointed, the field magnitude was obtained via

$$|\mathbf{E}|^2 = \left[\frac{E_x(i,j,k) + E_x(i-1,j,k)}{2}\right]^2 + \left[\frac{E_y(i,j,k) + E_y(i,j-1,k)}{2}\right]^2 + \left[\frac{E_z(i,j,k) + E_z(i,j,k-1)}{2}\right]^2 .$$

Among other approaches, the in-house code was validated by comparing whole-body averaged SAR values with those reported in [20], where a member of the Virtual Family was illuminated by a plane wave.

3. Results

3.1 Close-Proximity Dosimetry

In the simulations we performed, the highest SAR values were obtained when the human’s face was centered on the plane containing the dual-band antenna. This corresponds to an individual putting his or her face in close proximity to the meter but not centering the head, as would typically be done to look into the meter. Instead, the center of the head was displaced to the side, so as to align with the antenna.

Figure 3 shows color-map snapshots of the vertical component of the electric field taken from FDTD simulations where the members of the Virtual Family had their noses nearly aligned with the plane of the dual-band antenna. The field was displayed over a sagittal plane (i.e., the plane passed through the person from front-to-back, head-to-toe). In these snapshots, the color-mapping was such that the field magnitude is visible over three decades. As the color-bar shown in Figure 3d indicates, white corresponds to the maximum value, and as the fields decrease, they pass through the colors of the rainbow. Fields less than one one-thousandth of the maximum value appear as black. Since the electric field was zero within the antenna, the antenna could be seen as a black outline. The outline of the meter box was also visible as a black outline to the right of the antenna. The field was maximum in the immediate vicinity of the antenna. These snapshots were taken at time step 9,200 (i.e., they represented the instantaneous value of the field at that time). The frequency was 850 MHz.

Note that the members of the Virtual family did not all have their heads oriented the same way. Thus, although Mom and Dad had their noses as the forward-most body part, for Son and Daughter, the forward-most feature was the forehead. In Figure 3, the separations between the left-most segment of the antenna and the right-most feature of a family member were Dad, 19.5 mm; Mom, 27.0 mm; Daughter, 28.5 mm; and Son, 21.0 mm. For Daughter and Son, these separations were relative to the forehead, which was above the vertical center of the antenna. The nose for the children was roughly 7.5 mm further away horizontally.

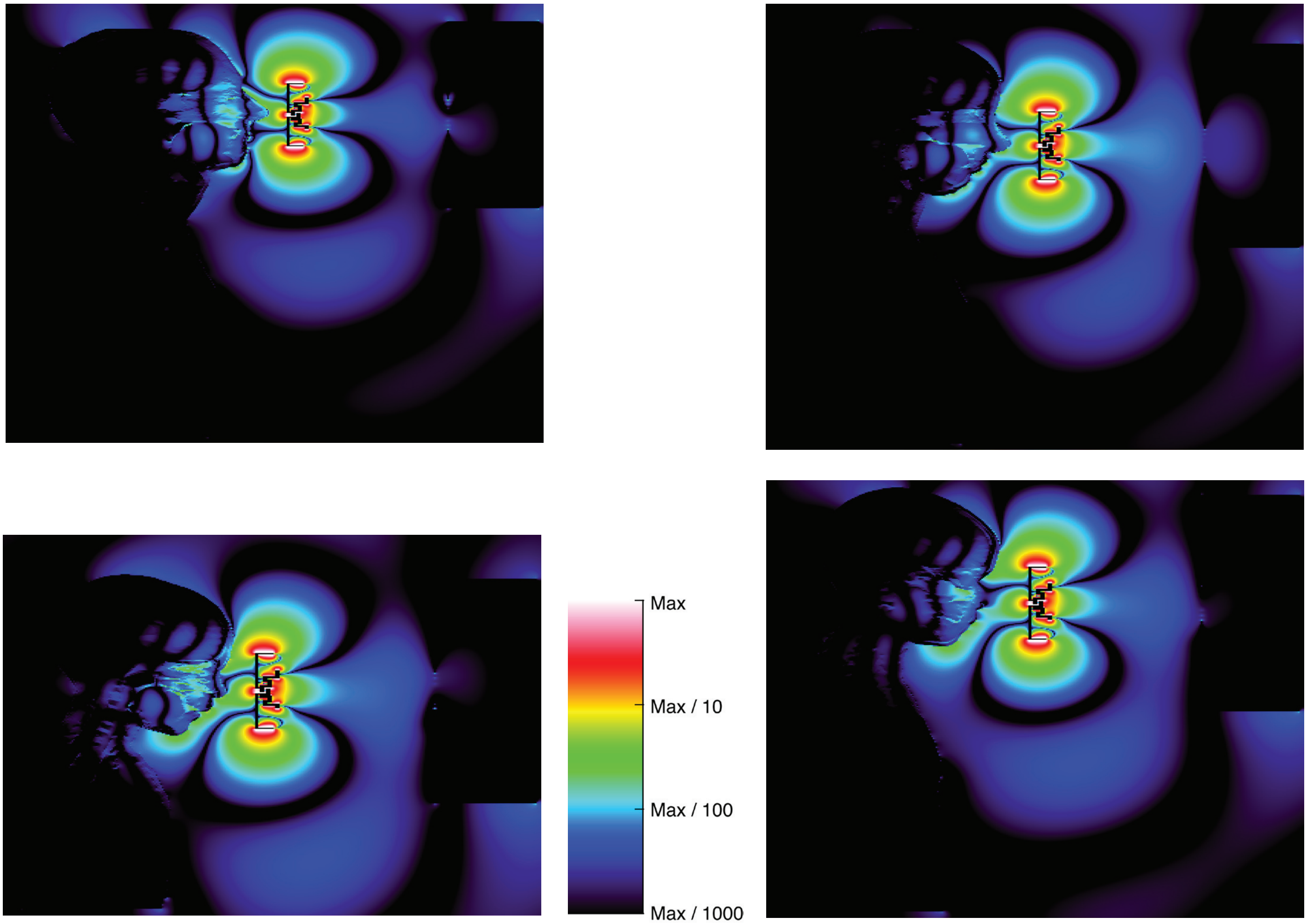

Figure 3. Color-map snapshots of the vertical component of the relative electric-field strength found in the sagittal plane containing the antenna: (a) Dad, (b) Mom, (c) Son, (d) a color bar showing the three-decade logarithmic scaling for all plots, (e) Daughter.

Rather than a two-dimensional slice, Figure 4 provides a three-dimensional representation of the 10 g averaged SAR obtained from the same simulations that are depicted in Figure 3. The SAR was visible only at the outer-most tissue. The same color mapping was used in Figures 3 and 4, but one should keep in mind that one figure shows field and the other shows SAR. In each figure, the normalization was to the maximum value present in that figure (numeric values follow). Clearly, the highest SAR values occurred at points closest to the center of the antenna, which, for these simulations, was the nose and the area surrounding the nose.

Table 1 shows the maximum 1 g, 10 g, and whole-body averaged SAR values obtained from these simulations at 850 MHz and 1900 MHz. The 10 g IEEE [38] guideline specifies a limit of 4.0 W/kg for the general public, and 20.0 W/kg for occupational exposure. The 1 g FCC limit is 1.6 W/kg for uncontrolled environments, and 8 W/kg for controlled environments [21]. The whole-body averaged SAR limit is 0.08 W/kg for uncontrolled environments. As might be expected for a finite source such as existed in these simulations, the whole-body SAR was generally well below the limit. The 1 g and 10 g values in the table exceeded the general-public/uncontrolled-environment limits. For 850 MHz, the 1 g and 10 g values fell below the occupational limits, but not for 1900 MHz. Recall that these values *do not* account for the actual duty cycle of these meters. To incorporate the duty cycle into these values, they should be multiplied by a factor of approximately 8.8×10^{-4}. By doing so, all values fell well below the general-public limits.

Simulations were also done where the human had his or her head centered about the meter (i.e., a position one might expect if the person were looking into the meter). This position moved the nose slightly further from the antenna than the scenario considered above. However, the separation between the human and the front of the meter was identical to that used before. (Note that the separations previously given were between the antenna and the human. As Figure 1 shows, the antenna is recessed in the meter by several millimeters. All of these measurements thus assumed that the human was closer to the meter than 28 mm.) Table 2 shows the corresponding maximum 1 g, 10 g, and whole-body averaged SAR values at 850 MHz and 1900 MHz. This slight shift in the position of the human relative to the antenna reduced the maximum values, in some cases by more than a factor of two.

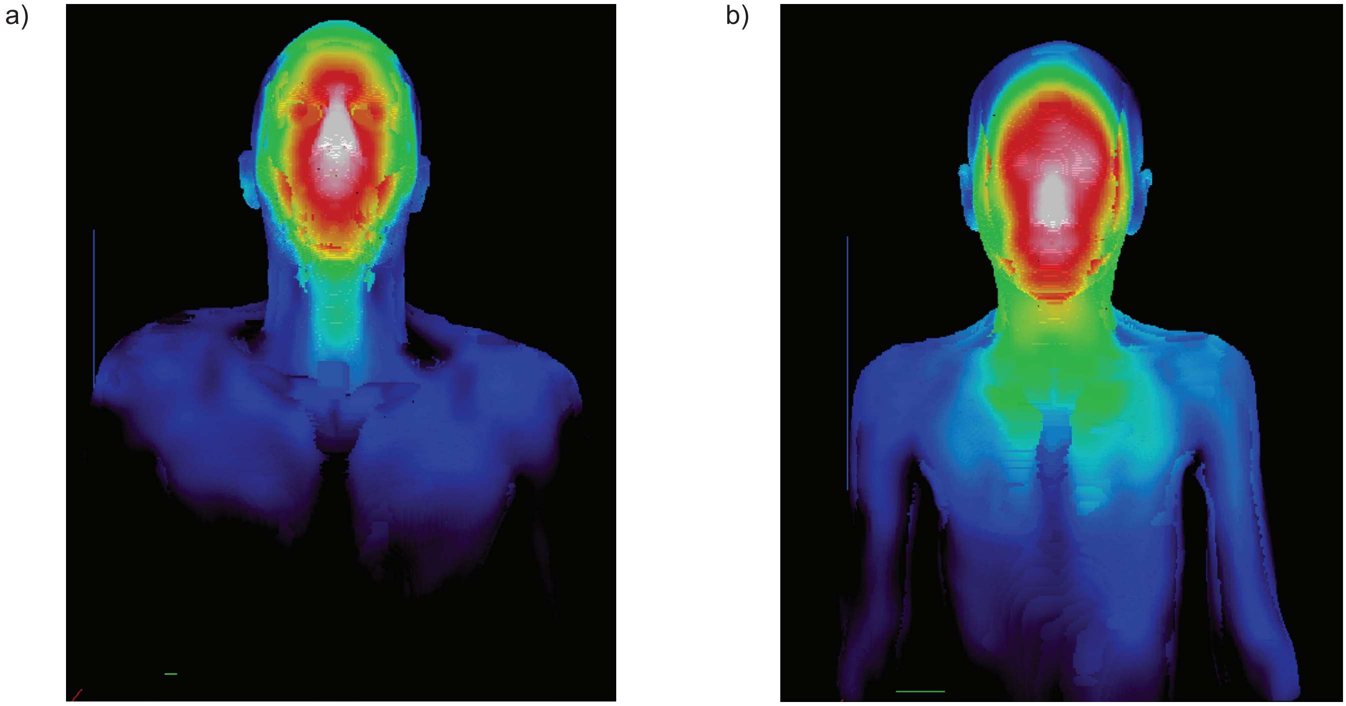

Figure 4. A three-dimensional depiction of the 10 g averaged SAR value at the outer-most tissue of the human. The results shown here were from the same simulations depicted in Figure 3. The same logarithmic color map was used as in the previous figure: (a) Dad, (b) Daughter.

Table 1. The SAR values for Virtual Family members corresponding to the simulations depicted in Figure 3. These values assumed continuous transmission, and did not account for the meter's actual duty cycle, which would reduce these values by a factor of approximately 1000.

	Dad	Mom	Daughter	Son
850 MHz, Whole Body	0.009	0.008	0.0150	0.0332
850 MHz, 10 g	1.64	1.32	1.30	1.45
850 MHz, 1 g	2.81	2.27	2.18	2.46
1900 MHz, Whole Body	0.014	0.0196	0.0252	0.0512
1900 MHz, 10 g	2.94	2.85	2.68	3.12
1900 MHz, 1 g	5.97	5.40	5.80	6.89

Table 2. The SAR values for the simulations where the head was centered about the meter. Continuous transmission was assumed.

	Dad	Mom	Daughter	Son
850 MHz, Whole Body	0.0063	0.0081	0.0137	0.0237
850 MHz, 10 g	0.51	0.76	0.90	0.70
850 MHz, 1 g	1.09	1.05	1.44	1.26
1900 MHz, Whole Body	0.013	0.0176	0.025	0.0454
1900 MHz, 10 g	1.16	1.42	1.44	1.05
1900 MHz, 1 g	1.72	2.59	3.11	2.08

Table 3a. SAR values for Dad when the separation between the antenna and nose was varied. Continuous transmission was assumed.

	6.75 cm	12.75 cm	18.75 cm	24.75 cm
850 MHz, Whole Body	0.0015	0.0009	0.0007	0.0005
850 MHz, 10 g	0.44	0.185	0.104	0.064
850 MHz, 1 g	1.016	0.449	0.257	0.16
1900 MHz, Whole Body	0.0045	0.004	0.0034	0.0029
1900 MHz, 10 g	1.138	0.656	0.424	0.277
1900 MHz, 1 g	2.03	1.184	0.761	0.499

Table 3b. SAR values for Mom when the separation between the antenna and nose was varied. Continuous transmission was assumed.

	7.2 cm	13.2 cm	19.2 cm	25.2 cm
850 MHz, Whole Body	0.0018	0.0011	0.0008	0.0006
850 MHz, 10 g	0.479	0.175	0.094	0.056
850 MHz, 1 g	0.779	0.284	0.153	0.092
1900 MHz, Whole Body	0.0073	0.0061	0.0047	0.0042
1900 MHz, 10 g	1.55	0.83	0.51	0.329
1900 MHz, 1 g	2.94	1.52	0.92	0.592

3.2 Dosimetry as a Function of Proximity

Table 3 gives the maximum 1 g, 10 g, and whole-body averaged SAR values for Dad and Mom at 850 MHz and 1900 MHz when the antenna was aligned with the nose as described above. However, here the horizontal separation was varied.

3.3 Dosimetry as a Function of the Position of the Antenna

3.3.1 Exposure and Vertical Displacement

Starting with the antenna aligned with the nose but 18 cm away horizontally for Dad, or 19.2 cm away for Mom, we kept the horizontal locations of the human and the meter the same, but calculated the SAR values when the meter was displaced downward in steps of 15 cm. The goal was to see if the exposure ever rose above what it was when the meter was directly in front of the nose. The whole-body SAR did increase slightly when the meter was more centrally located about the body, but the peak 1 g and 10 g values never increased above what they were when the meter was aligned with the nose. Table 4 shows the SAR values that were obtained. The 1 g SAR at 1900 MHz and a height of 0 cm was slightly above the limit, but all other values were below.

3.3.2 Exposure when Behind or Beside Meter

Figure 5 shows snapshots of the vertical component of the relative electric-field strength when Dad was behind the meter. (One can envision this as a scenario where the meter was mounted on a wall, and Dad was behind the wall. However, no actual wall was incorporated into this particular simulation, and hence the field Dad received was larger than it would otherwise have been. An analysis using measured fields of the attenuation of smart-meter RF fields caused by common residential walls can be found in [4].) In these snapshots, Dad appeared as the dark silhouette to the right. In Figure 5a, his nose was in the plane of the antenna, and was separated from the back of the meter by roughly 8.25 cm (which was less than the thickness of a typical wall). We called this position "behind" the meter. In Figure 5b, he was turned so that his back was toward the reader, his left shoulder was 9.45 cm from the back of the meter, and his head was roughly centered about the meter. We called this position "beside" the meter. Figure 5b provided a coronal slice through Dad. (All previous snapshots were sagittal slices.) The frequency was 850 MHz, and the snapshots were taken after 2000 time steps.

The maximum 1 g, 10 g, and whole-body averaged SAR values for the scenarios depicted in Figure 5 are given in Table 5 for 850 MHz and 1900 MHz. When the individual was beside the meter, the left shoulder was closest to the back of the meter a)

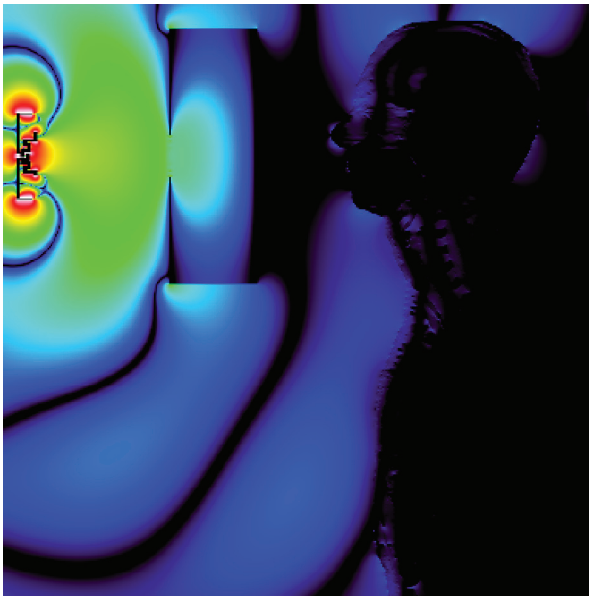

b)

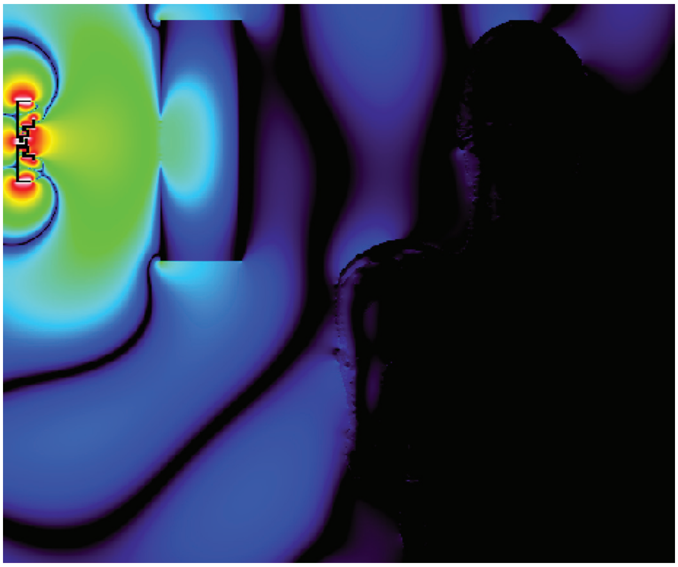

Figure 5. Snapshots of the vertical component of the relative electric-field strength at 850 MHz when Dad was: (a) behind the meter (and facing the meter), and (b) beside the meter (and facing away; coronal plane).

Table 4a. SAR values for Dad when the vertical position was varied. Continuous transmission was assumed.

	0 cm	15 cm	30cm	45 cm	60 cm	75 cm	90 cm
850 MHz, Whole Body	0.0007	0.0009	0.0007	0.0012	0.0007	0.0009	0.001
850 MHz, 10 g	0.104	0.047	0.022	0.028	0.026	0.041	0.033
850 MHz, 1 g	0.257	0.059	0.040	0.051	0.038	0.091	0.063
1900 MHz, Whole Body	0.0034	0.0044	0.0055	0.0055	0.0052	0.0047	0.0045
1900 MHz, 10 g	0.424	0.180	0.249	0.210	0.171	0.267	0.147
1900 MHz, 1 g	0.761	0.281	0.390	0.321	0.277	0.446	0.223

Table 4b. SAR values for Mom when the vertical position was varied. Continuous transmission was assumed.

	0 cm	15 cm	30 cm	45 cm	60 cm	75 cm	90 cm
850 MHz, Whole Body	0.0008	0.0010	0.0018	0.0015	0.0015	0.0016	0.0018
850 MHz, 10 g	0.094	0.043	0.071	0.033	0.021	0.03	0.030
850 MHz, 1 g	0.153	0.057	0.166	0.077	0.042	0.042	0.047
1900 MHz, Whole Body	0.0047	0.0063	0.0068	0.0077	0.0079	0.0078	0.0063
1900 MHz, 10 g	0.506	0.199	0.254	0.171	0.180	0.145	0.150
1900 MHz, 1 g	0.920	0.418	0.436	0.312	0.338	0.269	0.236

Table 5a. SAR values when an individual was behind the meter, as shown in Figure 5. Continuous transmission was assumed.

	Dad	Mom	Daughter	Son
850 MHz, Whole Body	0.00010	0.00015	0.00025	0.00030
850 MHz, 10 g	0.00175	0.00481	0.00235	0.00486
850 MHz, 1 g	0.00277	0.0107	0.00336	0.0092
1900 MHz, Whole Body	0.00025	0.00032	0.00048	0.00078
1900 MHz, 10 g	0.0057	0.0076	0.0064	0.0089
1900 MHz, 1 g	0.0090	0.0148	0.0135	0.0183

Table 5b. SAR values when an individual was beside the meter, as shown in Figure 5. Continuous transmission was assumed.

	Dad	Mom	Daughter	Son
850 MHz, Whole Body	0.00006	0.00014	0.00024	0.00023
850 MHz, 10 g	0.0037	0.0067	0.0096	0.00354
850 MHz, 1 g	0.0046	0.0098	0.0128	0.0083
1900 MHz, Whole Body	0.00012	0.00019	0.00027	0.00046
1900 MHz, 10 g	0.0103	0.0100	0.0131	0.0169
1900 MHz, 1 g	0.0141	0.0159	0.0183	0.0265

Table 6. SAR values when Dad or Mom were prone behind the meter. Continuous transmission was assumed.

	Dad	Mom	Daughter	Son
850 MHz, Whole Body	0.00027	0.00042	0.00066	0.00084
850 MHz, 10 g	0.0153	0.0210	0.0188	0.0266
850 MHz, 1 g	0.0306	0.0508	0.0406	0.0460
1900 MHz, Whole Body	0.00065	0.00090	0.00154	0.00227
1900 MHz, 10 g	0.0385	0.0482	0.0473	0.086
1900 MHz, 1 g	0.0679	0.0925	0.070	0.173

(and the nose was pointed 90° away from the front-to-back line of the meter). All values were far below the basic restrictions of the relevant exposure limits.

To model the possibility of somebody lying in a prone position on the other side of the wall from the meter, we considered a scenario similar to the geometry depicted in Figure 5b. However, the entire meter was rotated 90°. In this way, the orientation of the individual and the antenna were orthogonal to each other. One can think of this as looking down on a coronal plane containing the meter with Dad in a prone position. The meter was aligned with the head.

Table 6 shows the SAR values obtained for this "prone" scenario. Note that the SAR values were higher than they were when the orientation of the human and antenna were the same. This was explained by the added shielding provided by the meter box when the human and meter were aligned. In the prone scenario, more of the human was "out to the side" and thus exposed to stronger fields. Nevertheless, all the SAR values were well below the limits.

4. Conclusions

In this work, we considered the maximum possible exposure from one example of a wireless smart meter. Exposure to RF fields in both the 850 MHz and 1900 MHz bands were considered. The calculated values assumed that the antenna transmitted continuously, rather than using a typical duty cycle. Nevertheless, the SAR values that were obtained were within the safety guidelines, except in the contrived situation where an individual essentially placed his or her head against the meter. If the SAR values were reduced to take into account the 0.088% duty cycle [4], i.e., if the listed values were divided by a factor of approximately 1000, even when the human placed his or her head against the meter, the guidelines would be met. Vertical displacements of the meter relative to the body never produced greater peak 1 g and 10 g averaged SAR values than when the dual-band antenna was aligned with the nose.

In the somewhat more realistic scenarios, such as when the meter was directly to the side of the human or directly behind the human, the SAR values were well within the guideline basic restrictions. These simulations assumed free space between the human and the meter. (The existence of a wall would further reduce exposure.)

For the amount of power radiated by this finite source and the sizes of the family members, whole-body SAR values were substantially less than the safety guidelines, even when the body and meter were in close proximity.

5. Acknowledgment

The authors wish to think Prof. Robert Olsen of Washington State University and Richard Tell of Richard Tell Associates, Inc., for their support and helpful comments in the preparation of this work. The authors also acknowledge the Electric Power Research Institute (EPRI) for their financial support.

6. References

1. "Sebastopol Residents Lash Out Against PG&E Plan for 'Smart Meters'," *Sebastopol Press Democrat*, February 3, 2010.

2. "Sebastopol Crowd Decries PG&E's SmartMeters," *Sebastopol Press Democrat*, April 21, 2010.

3. "Sebastopol Urged to Ban SmartMeters," *Sebastopol Press Democrat*, September 21, 2010.

4. R. Tell, "An Investigation of Radiofrequency Fields Associated with the Itron Smart Meter," Electric Power Research Institute, Tech. Rep. 1021126, 2010, available at http://my.epri.com/portal/server.pt?Abstract_id=000000000001021126.

5. K. S. Yee, "Numerical Solution of Initial Boundary Value Problems Involving Maxwell's Equations in Isotropic Media," *IEEE Transactions on Antennas and Propagation*, **AP-14**, 3, March 1966, pp. 302-307.

6. A. Taflove and S. Hagness, *Computational Electrodynamics: The Finite-Difference Time-Domain Method, Third Edition*, Norwood, MA, Artech House, 2005.

7. A. Hadjem, D. Lautru, C. Dale, M. F. Wong, V. F. Hanna, and J. Wiart, "Study of Specific Absorption Rate (SAR) Induced in Two Child Head Models and in Adult Heads Using Mobile Phones," *IEEE Transactions on Microwave Theory and Techniques*, **53**, 1, January 2005, pp. 4-11.

8. M. Martínez-Búrdalo, A. Martín, M. Anguaiano, and R. Villar, "Comparison of FDTD-Calculated Specific Absorption Rate in Adults and Children when Using a Mobile Phone at 900 and 1800 MHz," *Physics in Medicine and Biology*, **49**, 2, 2004, pp. 345-354.

9. B. B. Beard, W. Kainz, T. Onishi, T. Iyama, S. Watanabe, O. Fujiwara, J. Wang, G. Bit-Babik, A. Faraone, J. Wiart, A. Christ, N. Kuster, A.-K. Lee, H. Kroeze, M. Siegbahn, J. Keshvari, H. Abrishamkar, W. Simon, D. Manteuffel, and N. Nikoloski, "Comparisons of Computed Mobile Phone Induced SAR in the SAM Phantom to that in Anatomically Correct Models of the Human Head," *IEEE Transactions on Electromagnetic Compatibility*, **48**, 2, May 2006, pp. 397-407.

10. J. Wang, O. Fujiwara, and S. Watanabe, "Approximation of Aging Effect on Dielectric Tissue Properties for SAR Assessment of Mobile Telephones," *IEEE Transactions on Electromagnetic Compatibility*, **48**, 2, May 2006, pp. 408-413.

11. A. Christ, M.-C. Gosselin, M. Christopoulou, S. Kühn, and N. Kuster, "Age-Dependent Tissue-Specific Exposure of Cell

Phone Users," *Physics in Medicine and Biology*, **55**, 2010, pp. 1767-1783.

12. A. Christ, M.-C. Gosselin, S. Kühn, and N. Kuster, "Impact of Pinna Compression on the RF Absorption in the Heads of Adult and Juvenile Cell Phone Users," *Bioelectromagnetics*, **31**, 5, July 2010, pp. 406-412.

13. M. Pelosi, O. Franek, M. B. Knudsen, G. F. Pedersen, and J. B. Andersen, "Antenna Proximity Effects for Talk and Data Modes in Mobile Phones," *IEEE Antennas and Propagation Magazine*, **52**, 2, June 2010, pp. 15-27.

14. M.-C. Gosselin, A. Christ, S. Kühn, and N. Kuster, "Dependence of the Occupational Exposure to Mobile Phone Base Stations on the Properties of the Antenna and the Human Body," *IEEE Transactions on Electromagnetic Compatibility*, **51**, 2, May 2009, pp. 227-235.

15. R. P. Findlay and P. J. Dimbylow, "SAR in a Child Voxel Phantom from Exposure to Wireless Computer Networks (Wi-Fi)," *Physics in Medicine and Biology*, **55**, 2010, pp. N405-N411.

16. M. Martínez-Búrdalo, A. Martín, A. Sanchis, and R. Villar, "FDTD Assessment of Human Exposure to Electromagnetic Fields from WiFi and Bluetooth Devices in Some Operating Situations," *Bioelectromagnetics*, **30**, 2009, pp. 142-151.

17. M. Martínez-Búrdalo, A. Martín, A. Sanchis, and R. Villar, "Comparison of SAR and Induced Current Densities in Adult and Children Exposed to Electromagnetic Fields from Electronic Article Surveillance Devices," *Physics in Medicine and Biology*, **55**, 2010, pp. 1041-1055.

18. R. P. Findlay and P. J. Dimbylow, "Effects of Posture on FDTD Calculations of Specific Absorption Rate in a Voxel Model of the Human Body," *Physics in Medicine and Biology*, **50**, 2005, pp. 3825-3835.

19. P. Dimbylow, W. Bolch, and C. Lee, "SAR Calculations from 20 MHz to 6 GHz in the University of Florida Newborn Voxel Phantom and their Implications for Dosimetry," *Physics in Medicine and Biology*, **55**, 2010, pp. 1519-1530.

20. J. F. Bakker, M. M. Paulides, A. Christ, N. Kuster, and G. C. van Rhoon, "Assessment of Induced SAR in Children Exposed to Electromagnetic Plane Waves Between 10 MHz and 5.6 GHz," *Physics in Medicine and Biology*, **55**, 2010, pp. 3115-3130.

21. F. C. Commission, *Guidelines for Evaluating the Environmental Effects of Radiofrequency Radiation*, FCC 96-326, 1996.

22. I. S. C. (R2008), *IEEE Recommended Practice for Measurements and Computations of Radio Frequency Electromagnetic Fields with Respect to Human Exposure to Such Fields, 100 kHz-300 GHz*, Institute of Electrical and Electronics Engineers, 2002, revision of IEEE Standard C95.3-1991.

23. V. G. Khurana, C. Teo, M. Kundi, L. Hardell, and M. Carlberg, "Cell Phones and Brain Tumors: A Review Including the Long-Term Epidemiologic Data," *Surgical Neurology*, **72**, 3, 2009, pp. 205-214.

24. M. Gaestel, "Biological Monitoring of Non-Thermal Effects of Mobile Phone Radiation: Recent Approaches and Challenges," *Biological Reviews*, **85**, 3, August 2010, pp. 489-500.

25. A. El Habachi, E. Conil, A. Hadjem, E. Vazquez, M. F. Wong, A. Gati, G. Fleury, and J. Wiart, "Statistical Analysis of Whole-Body Absorption Depending on Anatomical Human Characteristics at a Frequency of 2.1 GHz," *Physics in Medicine and Biology*, **55**, 2010, pp. 1875-1887.

26. J.-P. Bérenger, "A Perfectly Matched Layer for the Absorption of Electromagnetic Waves," *Journal of Computational Physics*, **114**, 2, 1994, pp. 185-200.

27. J. A. Roden and S. D. Gedney, "Convolution PML (CPML): An Efficient FDTD Implementation of the CFS-PML for Arbitrary Media," *Microwave and Optical Technology Letters*, **27**, 5, December 2000, pp. 334-339.

28. I. Laakso, S. Ilvonen, and T. Uusitupa, "Performance of Convolutional PML Absorbing Boundary Conditions in Finite-Difference Time-Domain SAR Calculations," *Physics in Medicine and Biology*, **52**, 23, 2007, pp. 7183-7192.

29. W. Gropp, E. Lusk, and A. Skjellum, *Using MPI: Portable Parallel Programming with the Message Passing Interface, Second Edition*, Boston, MA, MIT Press, 1999.

30. D. J. Robinson and J. B. Schneider, "On the Use of the Geometric Mean in FDTD Near-to-Far-Field Transformations," *IEEE Transactions on Antennas and Propagation*, **AP-55**, 11, November 2007, pp. 3204-3211.

31. A. Christ, W. Kainz, E. G. Hahn, K. Honegger, M. Zeffer, E. Neufeld, W. Rasher, R. Janka, W. Bautz, J. Chen, B. Kiefer, P. Schmitt, H.-P. Hollenbach, J. Shen, M. Oberle, D. Szczerba, A. Kam, J. W. Guag, and N. Kuster, "The Virtual Family – Development of Surface-Based Anatomical Models of Two Adults and Two Children for Dosimetric Simulations," *Physics in Medicine and Biology*, **55**, 2010, pp. N23-N38.

32. "Dielectric Properties of Body Tissues," http://niremf.ifac.cnr.it/tissprop/.

33. S. Dey and R. Mittra, "A Conformal Finite-Difference Time-Domain Technique for Modeling Cylindrical Dielectric Resonators," *IEEE Transactions on Microwave Theory and Techniques*, **47**, 9, September 1999, pp. 1737-1739.

34. R. Schechter, M. Kragalott, M. Kluskens, and W. Pala, "Splitting of Material Cells and Averaging Properties to

Improve Accuracy of the FDTD Method at Interfaces," *Applied Computational Electromagnetics Society Journal*, **17**, 3, 2002, pp. 1998-2008.

35. P. J. Dimbylow, A. Hirata, and T. Nagaoka, "Intercomparison of Whole-Body Averaged SAR in European and Japanese Voxel Phantoms," *Physics in Medicine and Biology*, **53**, 2008, pp. 5883-5897.

36. T. M. Uusitupa, S. A. Ilvonen, I. M. Laakso, and K. I. Nikoskinen, "The Effect of Finite-Difference Time-Domain Resolution and Power-Loss Computation Method on SAR Values in Plane-Wave Exposure of Zubal Phantom," *Physics in Medicine and Biology*, **55**, 2008, pp. 445-452.

37. I. Laakso, T. Uusitupa, and S. Ilvonen, "Comparison of SAR Calculation Algorithms for the Finite-Difference Time-Domain Method," *Physics in Medicine and Biology*, **55**, 2010, pp. N421-N431.

38. *IEEE Standard for Safety Levels with Respect to Human Exposure to Radio Frequency Electromagnetic Fields, 3 kHz to 300 GHz*, IEEE Std C95.1, 1999 Edition.

Introducing the Feature Article Authors

Lanchuan Zhou was born in Sichuan, China, in 1976. He received his BS in Electrical Engineering from the University of Electronic Science and Technology of China, and his MS in Electrical Engineering from the University of Twente, in 1999 and 2004, respectively. In 2012, he received his PhD from the School of Electrical Engineering and Computer Science at Washington State University. His primary research interest is in computational electromagnetics.

John B. Schneider received the BS in Electrical Engineering from Tulane University and the MS and PhD in Electrical Engineering from the University of Washington. Prof. Schneider is a former recipient of the Office of Naval Research Young Investigator Award, and was the co-Chair of the Technical Program Committee for the 2011 IEEE International Symposium on Antennas and Propagation. He is a Fellow of the IEEE.